Aerospace Science and Technology 124 (2022) 107526

Contents lists available at ScienceDirect

Aerospace Science and Technology

www.elsevier.com/locate/aescte

Numerical study of high temperature non-equilibrium effects of double-wedge in hypervelocity flow

Chunliang Dai [a], Bo Sun [a,*], Changfei Zhuo [a], Shengbing Zhou [b], Changsheng Zhou [a], Lianjie Yue [c]

[a] School of Mechanical Engineering, Nanjing University of Science and Technology, Nanjing 210094, China
[b] College of Aerospace Engineering, Chongqing University, Chongqing 400044, China
[c] State Key Laboratory of High-Temperature Gas Dynamics, Institute of Mechanics, CAS, Beijing 100190, China

ARTICLE INFO

Article history:
Received 21 September 2021
Received in revised form 11 March 2022
Accepted 27 March 2022
Available online 1 April 2022
Communicated by Qiulin Qu

Keywords:
Hypervelocity double-wedge flow
High temperature non-equilibrium effects
Laminar and turbulence flow
Shock wave interaction
Shock wave/boundary layer interaction

ABSTRACT

The high temperature non-equilibrium effects of shock wave interaction and shock wave/boundary layer interaction are important issues for hypervelocity flows. The models of thermochemical non-equilibrium gas (TCNEG), thermal non-equilibrium chemical frozen gas (TNCFG), chemical non-equilibrium gas (CNEG), and thermally perfect gas are used to simulate the double-wedge flows with a total enthalpy of 8 MJ/kg in this study. The unsteady two-temperature Naiver-Stokes equations in the laminar and turbulence flows are solved using the finite volume method. For laminar flow, the shock structures and the heat flux peak for TCNEG model at 170 μs are agreed better with the experiment result compared to reference studies. There are different size vortices in the separation zones, which causes the distributions of the wall heat flux oscillate irregularly. The thermal non-equilibrium effects are the most intense near the attached shock and detached shock, and the degree of oxygen dissociation is the strongest in the subsonic zone near the slip-line. For turbulence flow, the shock structures for the four models are close to Edney's IV interaction. The separation shock position for the TNCFG model is the most upstream, and that for the CNEG model is quite different from the TCNEG model. The intensity of the reflected shocks on the back wedge and its nearby shock interaction largely determine the peak values of the heat flux for the four models.

1. Introduction

Shock wave interaction (SWI) and shock wave/boundary layer interaction (SWBLI) are common physical phenomena in the hypersonic flows such as scramjets, reentry vehicles, and launch vehicles, which may cause the local high temperature and unsteady oscillation of the vehicle surfaces [1–3]. A large separation zone caused by SWBLI can cause "flow choking" in the channel of the scramjet inlet [4–6], and even cause the inlet to unstart, affecting the normal operation of the engine [7–10]. Therefore, the accurate predictions of SWI and SWBLI are very crucial for the design of a hypersonic vehicle. A double-wedge configuration is often used to design the scramjet inlet [11,12], so it is selected to study the high temperature non-equilibrium effects of SWI and SWBLI in the hypervelocity flow.

Different from the low-enthalpy supersonic or hypersonic flows, the chemical reaction and vibrational non-equilibrium can not be ignored in the high-enthalpy flow. A high total temperature in the hypervelocity flow can excite the energies of molecular rotational, vibrational, and electronic energy. Then, the gas molecules in the shock-layer may undergo the dissociation and ionization reactions. The above phenomena are known as the "high temperature non-equilibrium effects", including the chemical non-equilibrium and thermochemical non-equilibrium effects [13]. Therefore, the SWI and SWBLI in the high-enthalpy and hypervelocity flows are complex and worthy of further study.

The SWI and SWBLI in the low-enthalpy supersonic or hypersonic flows have been widely studied [14–16], which will not be introduced here. In 2012, Swantek carried out a series of wind tunnel experiments on the hypervelocity flows of double-cone and double-wedge [17]. The static pressure and heat flux measured in the experiment are often used for the numerical verification. The wind tunnel experiments are difficult to reproduce the hyperveloc-

---

* Corresponding author.
E-mail address: hypersun@126.com (B. Sun).

https://doi.org/10.1016/j.ast.2022.107526
1270-9638/

Nomenclature

Variables

h_0	total enthalpy	J/kg
Re	Reynolds number	m^{-1}
t	time	s
ρ	density	kg/m^3
T	static temperature	K
D	molar diffusion coefficient	m^2/s
y	mole fraction	1
$\dot{\omega}$	mass generation rate of component	$kg/m^3{\cdot}s$
P	static pressure	Pa
u	velocity	m/s
τ	shear stress tensor	
E	energy	J/kg
H	enthalpy	J/kg
q	heat flux	W/m^2
N_m	number of molecular species	

Subscripts

s	species
∞	free stream
i, j	direction
k	reaction order
ve	vibrational-electronic-electron
tr	translational-rotational

Abbreviation

SWI	shock wave interaction
SWBLI	shock wave/boundary layer interaction
TCNEG	thermochemical non-equilibrium gas
TNCFG	thermal non-equilibrium chemical frozen gas
CNEG	chemical non-equilibrium gas
TPG	thermal perfect gas
HLLC	Harten-Lax-van Leer contact
TVD	Total Variation Diminishing

ity flow environments, so most studies about the SWI and SWBLI in the hypervelocity flow were finished by numerical simulation. Hao [18] simulated the two-dimensional and three-dimensional unsteady flows of 30°-55° double-wedge with the total enthalpy of 8.0 MJ/kg. For the nitrogen flow, it is found that the separation zone and the surface heat flux peak in the three-dimensional simulations are smaller. The shock wave interaction mechanism in air is similar to that in nitrogen. The real-gas effects tend to decrease the separation bubble and reduce the standoff distance of the detached shock induced by the second wedge, resulting in a lower surface peak heat flux. The flows over double-wedges with four aft angles in air with a total enthalpy of 8.0 MJ/kg were simulated by Vatansever, using hyperReactingFoam, a open-source non-equilibrium solver [19]. And, the two numerical results are compared qualitatively and quantitatively with the experiment [17]. He found that there was chemical frozen flow downstream of the expansion corner. The wall heat flux and static pressure increased with the increase of the aft angle. Fluctuations of the wall heat flux and static pressure distribution with time increase significantly along the second wedge when the aft angle is higher. The unsteady flows of the double-wedge for different gas compositions were predicted by Tumuklu, using the direct-simulation Monte Carlo and window proper orthogonal decomposition methods [20]. He found that the thermochemical non-equilibrium effects can change the shock structure, the size of the separation zone, and the time required to reach a steady state. The heat flux and detached shock standoff distance are qualitatively consistent with experiments [17] where the freestream density is eight times higher than his calculation.

Overall, the wall heat flux peaks of the double-wedge obtained in the above studies are much lower than the experimental value [17], and their positions are also deviated markedly from the experiment. Most of the numerical studies on the double-wedge flow mainly focus on the comparison of numerical results and experimental data [18–20], instead of analyzing the mechanism of the high temperature non-equilibrium effects in the double-wedge flows. So, more numerical simulations of the double-wedge in the hypervelocity flows are needed. The hypervelocity double-wedge flows were assumed to be laminar to explain the external flow of reentry vehicles in most studies. Yet, the laminar flow assumption is not suitable for the internal flows of the high Mach number scramjet inlet, which may involve shock wave/turbulent boundary layer interaction [7–10]. Hence, it is necessary to study the high temperature non-equilibrium effect of the hypervelocity turbulence flows.

To better understand the high temperature non-equilibrium effects of the SWI and SWBLI in the hypervelocity flow, the unsteady laminar double-wedge flows with total enthalpy of 8.0 MJ/kg are simulated by using four gas models. Then, the Spalart-Allmaras turbulence model is used to predict the hypervelocity double-wedge flows, which provides a reference for understanding the shock wave/turbulent boundary layer interaction in the high Mach number internal flow. The main structure of this study is as follows: the introduction of double-wedge model, numerical simulation method, and validation are given in Sec. 2. The analysis of the double-wedge flow fields and wall parameters are provided in Sec. 3. The conclusions of this study are presented in Sec. 4.

2. Experimental model and calculation method

2.1. Description of experiment

The experimental model and geometry of the double-wedge are shown in Fig. 1. The fore and aft angles of the wedge are equal to $\theta_1 = 30°$ and $\theta_2 = 55°$, respectively [17]. The lengths of the first and second surfaces are equal to $L_1 = 0.0508$ m and $L_2 = 0.2540$ m, respectively. The straight section length L_3 is 0.0108 m. The free-stream conditions selected in this study are as follows: velocity $u_\infty = 3812$ m/s, static temperature $T_\infty = 710$ K, static pressure $p_\infty = 780$ Pa, density $\rho_\infty = 0.0038$ kg/m^3, total enthalpy $h_0 = 8.0$ MJ/kg, unit Reynolds number $Re = 4.35 \times 10^5$ m^{-1}. The mass fractions of nitrogen and oxygen are 0.79 and 0.21, respectively. The flow is assumed to be laminar.

2.2. Governing equations

Based on different gas model assumptions, the following four models are used to predict the flows of the double-wedge: 1) thermal non-equilibrium with the finite rate chemical reactions, expressed as thermochemical non-equilibrium gas (TCNEG); 2) thermal non-equilibrium without chemical reactions, expressed as thermally non-equilibrium chemical freezing gas (TNCFG); 3) thermal equilibrium with the finite rate chemical reactions, expressed as chemical non-equilibrium gas (CNEG); 4) thermal equilibrium without chemical reactions, expressed as thermally perfect gas (TPG).

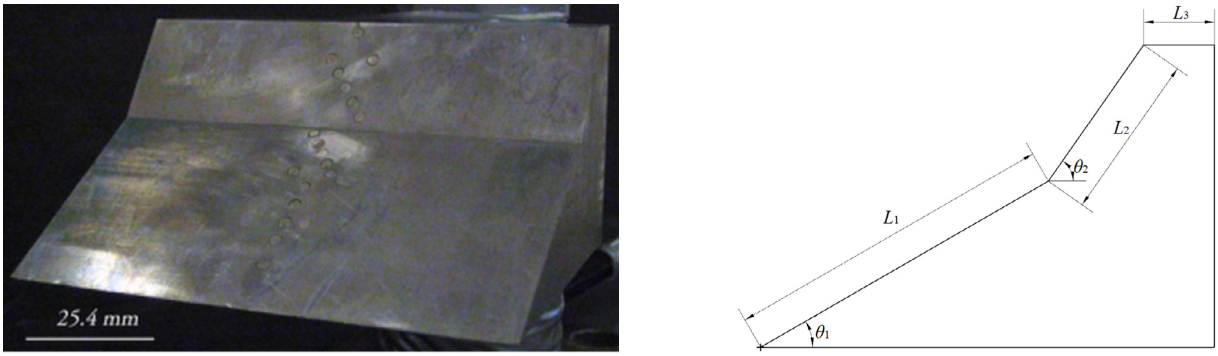

(a) Experimental model

(b) Geometric configuration

Fig. 1. Double-wedge model.

The multi-component compressible Naiver–Stokes equations are used for the hypervelocity flows in this study. The different internal energy states of molecules are expressed by a uniform temperature for the thermal equilibrium gas models. The conservation equations of mass, momentum, and energy can be expressed as follows:

$$\frac{\partial \rho_s}{\partial t} + \frac{\partial \rho_s u_i}{\partial x_i} = \frac{\partial}{\partial x_i}(\rho D_s \frac{\partial y_s}{\partial x_i}) + \dot{\omega}_s \tag{1}$$

$$\frac{\partial \rho u_i}{\partial t} + \frac{\partial \rho u_i u_j}{\partial x_j} = -\frac{\partial P}{\partial x_i} + \frac{\partial \tau_{ij}}{\partial x_j} \tag{2}$$

$$\frac{\partial \rho E}{\partial t} + \frac{\partial \rho H u_i}{\partial x_i} = \frac{\partial \tau_{ij} u_j}{\partial x_i} + \frac{\partial q_i}{\partial x_i} \tag{3}$$

where t is the time term; ρ_s, D_s, y_s, and $\dot{\omega}_s$ are the density, diffusion coefficient, mole fraction, and mass generation rate of component s, respectively; ρ and P are the density and static pressure of the mixture, respectively; x_i is the i-th axis coordinate; u_i and u_j are the velocity components in the i and j directions, respectively; τ_{ij} is each component of the shear stress tensor; E and H are the total energy and total enthalpy of the mixture per unit mass, respectively; q_i is the heat flux component in the i direction. The flow-field of the double-wedge for the TPG and CNEG models can be predicted by solving the above equations.

The Park's two-temperature model is used to describe the thermal non-equilibrium state [21]. This model assumes that the electron translational mode is equilibrium with the molecular vibrational mode, the low-lying electronic states of heavy particles are equilibrium with the ground electronic state at the electronic temperature. The vibrational-electronic temperature T_{ve} is used to describe the vibrational-electronic-electron mode including molecular vibrational energy, electronic excitation energy, and electron translational energy. The molecular translational-rotational mode is described using the translational-rotational temperature T_{tr}. To model the translational-rotational energy and vibrational-electronic-electron energy states separately, an additional energy conservation equation for vibrational-electronic-electron state need to be solved, and this energy conservation equation is given as the following

$$\frac{\partial(\rho e_{ve})}{\partial t} + \frac{\partial(\rho e_{ve} u_i)}{\partial x_i} = \frac{\partial}{\partial x_i}(q_{ve,i} + \sum_{s=1}^{N_m} \rho D_s e_{ve,s} \frac{\partial y_s}{\partial x_i}) + \omega_{ve} \tag{4}$$

where e_{ve} is the vibrational-electronic-electron energy of the mixture; $q_{\mathrm{ve},i}$ is the vibrational-electronic-electron heat flux component in the i direction; $e_{\mathrm{ve},s}$ and D_s are the vibrational-electronic-electron energy and diffusion coefficient of component s, respectively; N_m is the number of molecular species; ω_{ve} is the vibrational-electronic-electron energy term of the mixture, which can be expressed as $\omega_{ve} = e_{tv} + \sum_s \dot{\omega}_s e_{ve,s}$, e_{tv} is the relaxation energy between the translational and vibrational states, which can be expressed by the Landau-Teller equation with the high-temperature correction of Park [22].

The total energy conservation equation of the thermal non-equilibrium state is:

$$\frac{\partial(\rho E)}{\partial t} + \frac{\partial(\rho H u_i)}{\partial x_i} = \frac{\partial}{\partial x_i}\left(\tau_{ij} u_i + q_{tr,i} + q_{ve,i} + \sum_{s=1}^{N_s} \rho H_s D_s \frac{\partial y_s}{\partial x_i}\right) \tag{5}$$

where $q_{\mathrm{tr},i}$ is the translational-rotational heat flux component in the i direction; N_s and H_s are the total number and enthalpy of component s, respectively. The flow-field of the double-wedge for the TCNEG and TNCFG models can be predicted by solving equations (1), (2), (4), and (5).

2.3. Chemical kinetic model

As shown in Table 1, the chemical reaction mechanism including seven species (N_2, O_2, NO, N, O, NO^+, and e) and six elementary reactions is selected to model the reacting air [23]. A_k, β_k, k, E and R represent the pre-exponential factor, temperature index, reaction order, reaction activation energy, and gas constant, respectively. M is the third collision body in the first three elementary reactions, and the specific values are shown in Table 2.

All the chemical reaction rates k_c are calculated by Arrhenius formula, which can be expressed as $k_c = A_k T_c^{B_k} \exp(-E T_c^{-1})$. The backward reaction rates are obtained by the equilibrium constant, which are calculated from Gibbs energy fitted by McBride et al. [24]. According to Park's two-temperature model [21], the control temperature T_c of chemical reaction is a function of the translational-rotational and vibrational-electronic temperatures. It can be expressed as $T_c = {T_{\mathrm{tr}}}^n {T_{\mathrm{ve}}}^{1\text{-}n}$. n is 0.5 in the dissociation reactions, and n is 0 in the reactions with electron participation; n is 1 in other reactions.

2.4. Turbulence model

The one equation Spalart-Allmaras (S-A) turbulence model [25] has successfully predicted the flow and combustion of the Mach 12 scramjet [26–28], it was widely used for the subsonic airfoil flow as well [29,30]. Hence, the Reynolds-averaged Navier-Stokes (RANS) equations are closed using this turbulence model to simulate the double-wedge flow-field in the turbulent flows. The near-wall region compressible equation is as follows:

Table 1
Finite rate chemical reaction model including six elementary reactions.

Reaction	A_k ($m^3 \cdot mol^{-1} \cdot s^{-1}$)	β_k	E/R ($kJ \cdot mol^{-1}$)	n-forward	n-backward
$N_2 + M \leftrightarrow 2N + M$	7.0E+18	-1.6	9.411448×10^8	0.5	1
$O_2 + M \leftrightarrow 2O + M$	2.0E+18	-1.5	4.94683×10^8	0.5	1
$NO + M \leftrightarrow N + O + M$	5.0E+12	0.0	6.27707×10^8	0.5	1
$NO + O \leftrightarrow N + O_2$	8.4E+09	0.0	1.617073×10^8	1	1
$N_2 + O \leftrightarrow N + NO$	6.4E+14	-1.0	3.1292576×10^8	1	1
$N + O \leftrightarrow NO^+ + e$	8.8E+14	1.0	2.652166×10^8	1	0

Table 2
Third collision body M in reactions.

Reaction	Species (e)	Species (N)	Species (O_2)	Species (NO)	Species (O)	Species (NO+)	Species (N_2)
1	1750	4.286	1.0	1.0	4.286	1.0	1.0
2	0.0	5.0	1.0	1.0	5.0	1.0	1.0
3	0.0	22	1.0	22	22	1.0	1.0

$$\frac{\partial \rho\tilde{\nu}_t}{\partial t}+\frac{\partial \rho\tilde{\nu}_t u_i}{\partial x_i}=c_{b1}\, S\, \rho\tilde{\nu}_t - c_{w1} f_w \rho\left(\frac{\tilde{\nu}_t}{d}\right)^2+\frac{1}{\sigma}\frac{\partial}{\partial x_i}\left(\mu\frac{\partial\tilde{\nu}_t}{\partial x_i}\right)+\frac{1}{\sigma}\frac{\partial}{\partial x_i}\left(\sqrt{\rho}\tilde{\nu}_t\frac{\partial\sqrt{\rho}\tilde{\nu}_t}{\partial x_i}\right)+\frac{c_{b2}}{\sigma}\frac{\partial\sqrt{\rho}\tilde{\nu}_t}{\partial x_j}\frac{\partial\sqrt{\rho}\tilde{\nu}_t}{\partial x_j} \tag{6}$$

where $\tilde{\nu}_t$, S are the turbulent eddy viscosity and the magnitude of the vorticity, separately; f_w and c_{w1} are non-dimensional functions; σ, c_{b1}, and c_{b2} are constants. The above specific values and functions in the S-A turbulence model can be found in the reference [25].

2.5. Numerical algorithm and boundary condition

The system of equations is numerically using the finite volume method. The thermal properties can be expressed in the polynomial forms [31]. The bulk viscosity and thermal conductivity are computed by applying Sutherland's Law to each species. The mixture transport properties can be computed using Wilke's Law [32]. The diffusion coefficient is determined using a Schmidt number. The inviscid flux is calculated using a approximate Riemann solver named Harten-Lax-van Leer contact (HLLC) [33], and a second-order multi-dimensional Total Variation Diminishing (TVD) polynomial interpolation is determined by finite reconstruction of the cell center [34]. The continuous limiter and multi-grid approach are used to improve convergence. A second-order point implicit scheme with dual time-stepping is used to time integration. The above calculation method has been used for simulating the flows of a high-enthalpy cylinder and a Mach 12 inward-turning inlet [13]. For the unsteady flow in present study, the time step for the calculations is 5.0×10^{-8}. The maximum number of internal iterations is 30 to ensure that the numerical residuals are reduced by at least 2-3 orders of magnitude. From reference [17], the separated shock continues to traverse upstream on the front wedge until approximately 170 μs, so the calculation results at 170 μs were mainly analyzed in this study.

As shown in Fig. 2, the calculation domain is divided into the structured grids with normal spacing of 1.0×10^{-7} m at the surfaces. The wedge surfaces are assumed to be no-slip, non-catalytic, and 300 K isothermal walls. The parameters in the inflow boundary are selected to initialize all calculations. For thermal non-equilibrium flow simulations, the vibrational-electronic temperature of the inflow boundary is equal to the static temperature.

2.6. Validation of method

The numerical results for the TCNEG model are selected for the present numerical validation. Firstly, the computational domains with the three types of grids are solved to verify the convergence of the grids. The nodes of the coarse grids, fine grids, and dense grids are 300 × 300, 300 × 500, and 340 × 550, respectively. As shown in Fig. 3, the wall parameters of the fine and dense grids are basically the same. The peak values of wall static pressure and heat flux with coarse grids are lower than those of others. The wall heat flux of fine grids and dense grids are in good agreement with the experiment. Considering the computational efficiency, the computational domain with the fine grids is used for the following study.

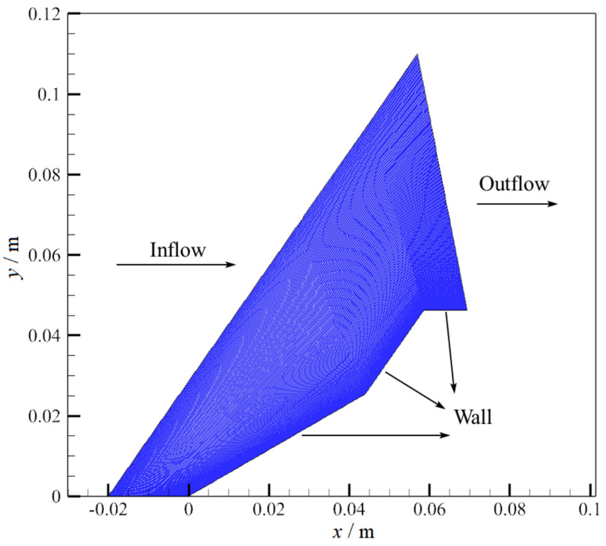

Fig. 2. Calculation domain of double-wedge.

The results of the experimental study of Swantek [17], numerical study of Vatansever et al. [19] and Komives et al. [35] are selected to validate the present calculation method. To examine the uniformity of the double-wedge flow-field at 160 μs, we compared the density gradient for the TCNEG model with the experimental schlieren diagram of Swantek, the numerical schlieren diagram of Vatansever et al. and Komives et al. As shown in Fig. 4, the location of detached shock and triple point for the TCNEG model are closer to upstream than experiment [17], but those are closer to the numerical results of Vatansever et al. and Komives et al. The position of the separated shock for the TCNEG model is closer to the upstream than the experiment [17] and Komives et al., while that is close to Vatansever et al. Overall, the shock structures for the TCNEG model are broadly consistent with both the experiment study and the reference numerical studies.

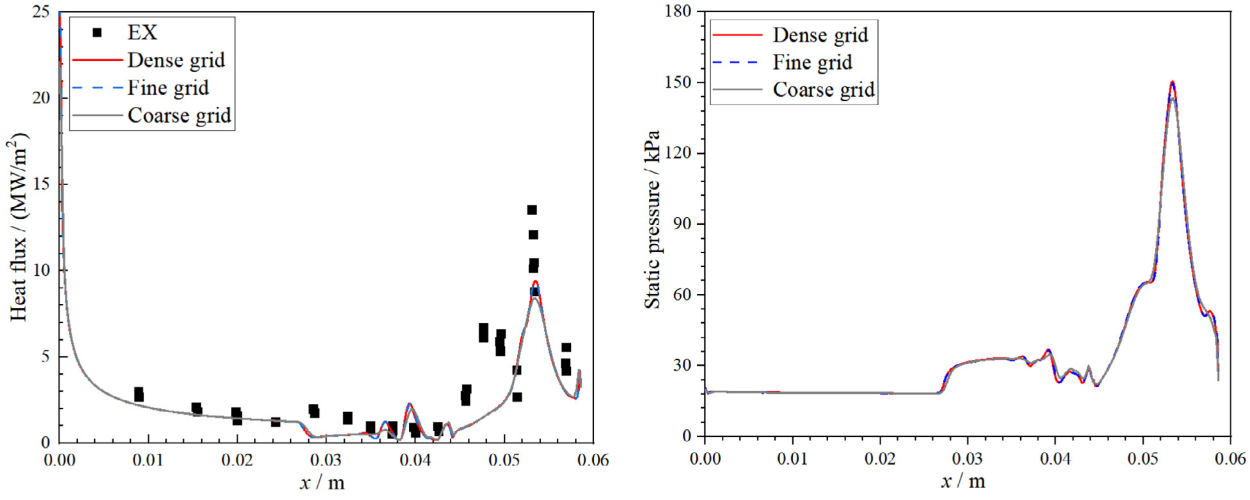

(a) Heat flux

(b) Static pressure

Fig. 3. Wall parameters for TCNEG model with different grids.

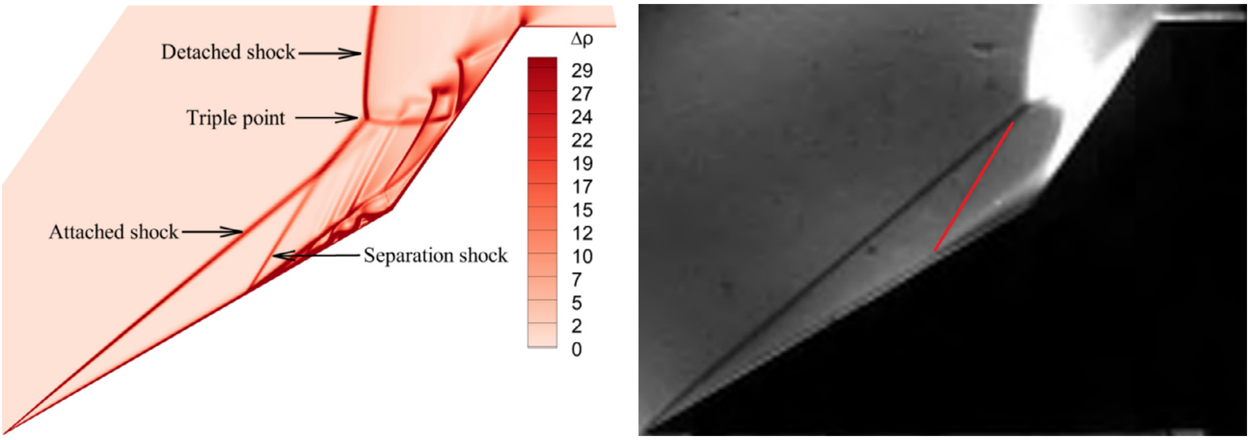

(a) Density gradient for TCNEG model at 160 μs

(b) Experimental schlieren diagram at 160 μs [17]

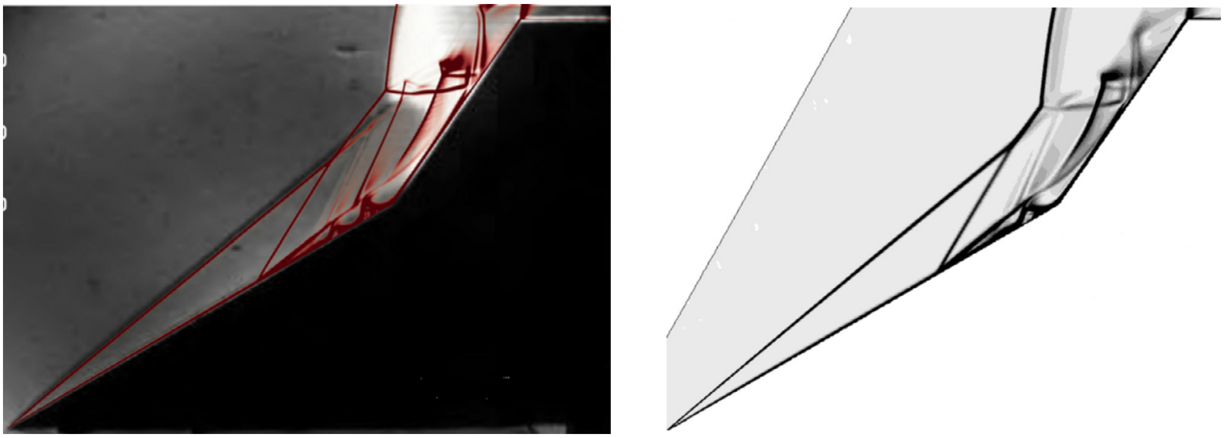

(c) Numerical schlieren diagram of Vatansever at 160 μs [19]

(d) Numerical schlieren diagram of Komives at 160 μs [35]

Fig. 4. Comparisons of flow-field at 160 μs.

As the experimental results of Swantek [17] shown, the position of the separated shock seemly no longer change at 170 μs, so it is essential to examine the uniformity of the double-wedge flow-field at 170 μs. From Fig. 5, the positions of the detached shock, triple point, and attached shock for the TCNEG model are close to those of experiment. Yet, the separated shock position for the TCNEG model is closer to the upstream than experiment, the cause of the above deviation may be that the three dimensional effects are not considered in the present study.

Similar to many cases in the reference [2], the wall heat flux at a certain moment is used for comparing with the experimental result. Fig. 6 shows the comparisons of the wall heat flux for the TCNEG models at different instants with experiment [17] and reference studies (Vatansever et al. [19] and Komives et al.

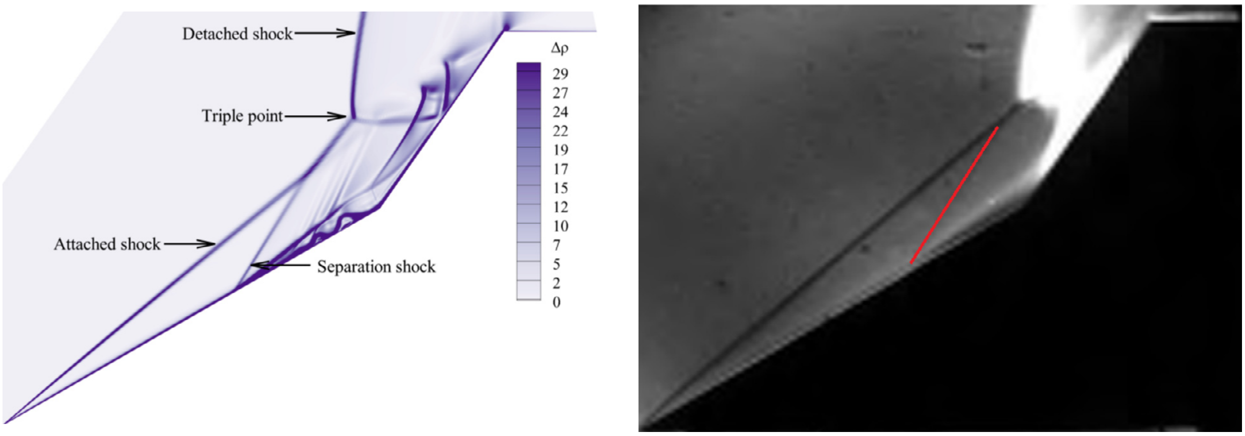

(a) Density gradient for the TCNEG model at 170 μs

(b) Experimental schlieren diagram at 170 μs

Fig. 5. Comparison of flow-fields at 170 μs.

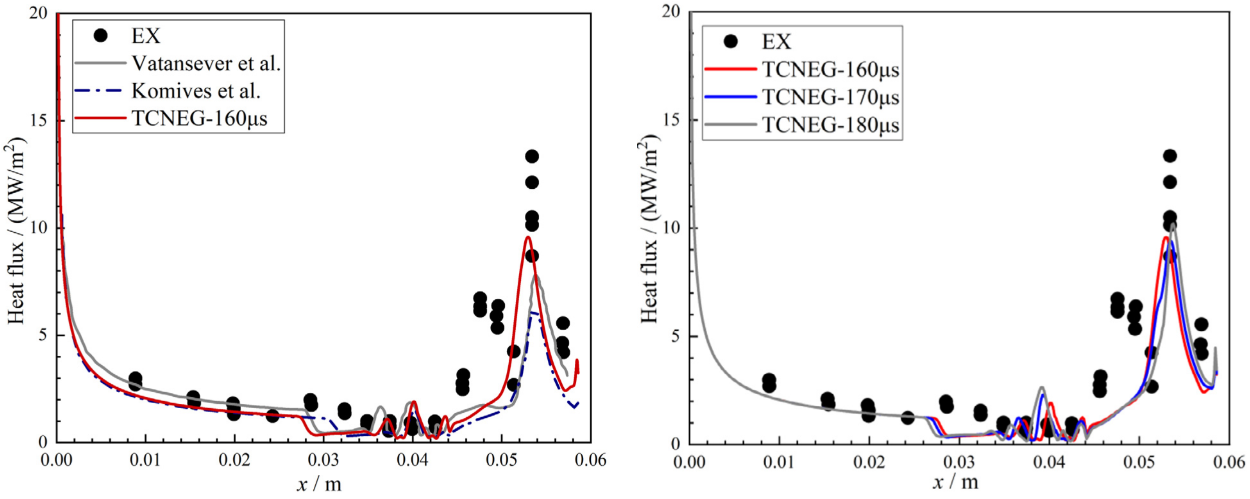

(a) Heat flux of TCNEG model, experiment and reference

(b) Heat flux of TCNEG model at different instants

Fig. 6. Comparisons of the wall heat flux for the TCNEG model at different instants with experiment and reference studies. (The heat flux of the experiment and reference studies are at 160 μs.)

[35]). Notably, the values of the wall heat flux from the experiment and reference studies are at 160 μs. From Fig. 6(a), the heat flux of the back wedge in reference studies is lower than the experimental value, the values of their peak heat flux are no more than 8.0 MW/m^2, which obviously deviates from the experiment. Compared to the reference studies, the wall heat flux of the two wedges for the TCNEG models at 160 μs is close to the experiment. Especially, the value of the peak heat flux for the TCNEG model at 160 μs is about 25.5%∼56.85 higher than the reference studies. The reason for the above difference should be the reacting air model without the backward reactions in the reference studies, and might also be the different transport properties and first mesh thickness.

From Fig. 6(b), the separation shock position slightly moves upstream with the increase of time, the numerical simulations have not reached steady state at 170 μs, which is similar to the situation of the reference [2,18,19]. Although the values of heat flux peak at 160 μs and 180 μs are higher than that at 170 μs, the positions of their heat flux peak are slightly deviated from the experiment. Importantly, the peak position of the heat flux for the TCNEG model at 170 μs is consistent with the experiment, its peak value is about 21.89%∼52.76% higher than the reference studies, so the double wedge flows at 170 μs will be mainly analyzed in the present study. Overall, the scale of separation zone for the TCNEG model is larger than that for the experiment [17]. However, the present calculation method performs better in predicting the aerodynamic loading.

3. Results and discussion

3.1. Analysis of flow-field in laminar flow

From Fig. 7(a), the attached shock formed by the front wedge intersects with the detached shock formed by the back wedge at the triple point to form the transmitted shock. The transmitted shock impinges on the back wedge, forming a reflected shock and causing a strong adverse pressure gradient, so there is a separation zone at the compression corner. The separation shock induced by the separation zone intersects with the attached shock and merges into a stronger shock, which changes the position of the triple point, the intensity of the transmitted shock, and shock interaction. The different sizes vortices inside the separation zone make its the slip surface uneven, forming several weak shocks and expansion waves. The detached shock is closer to a normal shock, and there is a subsonic region (red sonic line) downstream of it.

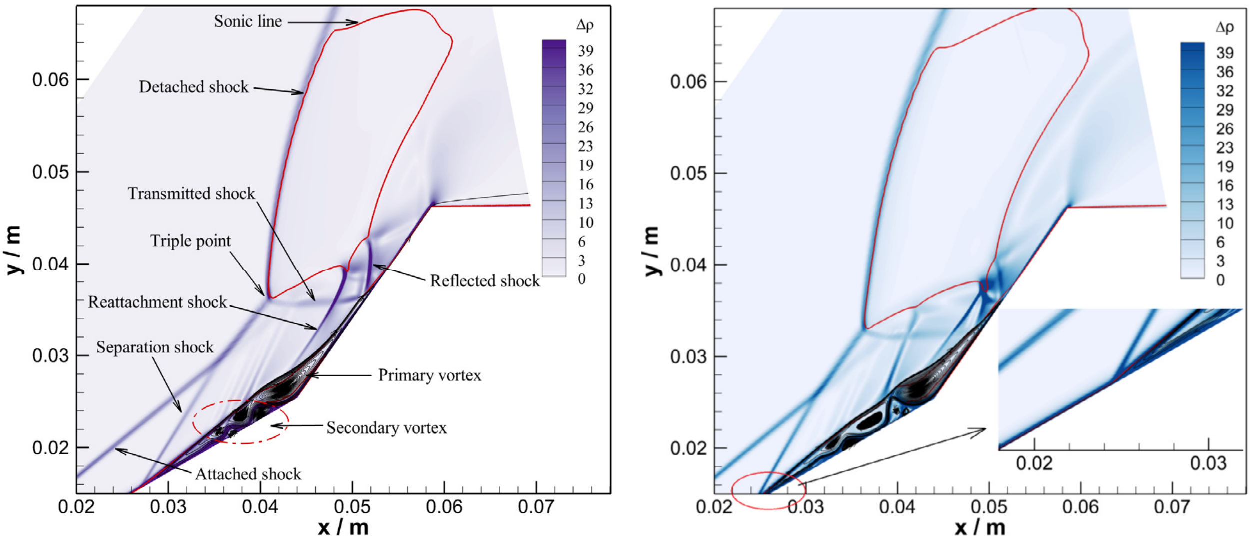

(a) TCNEG

(b) TNCFG

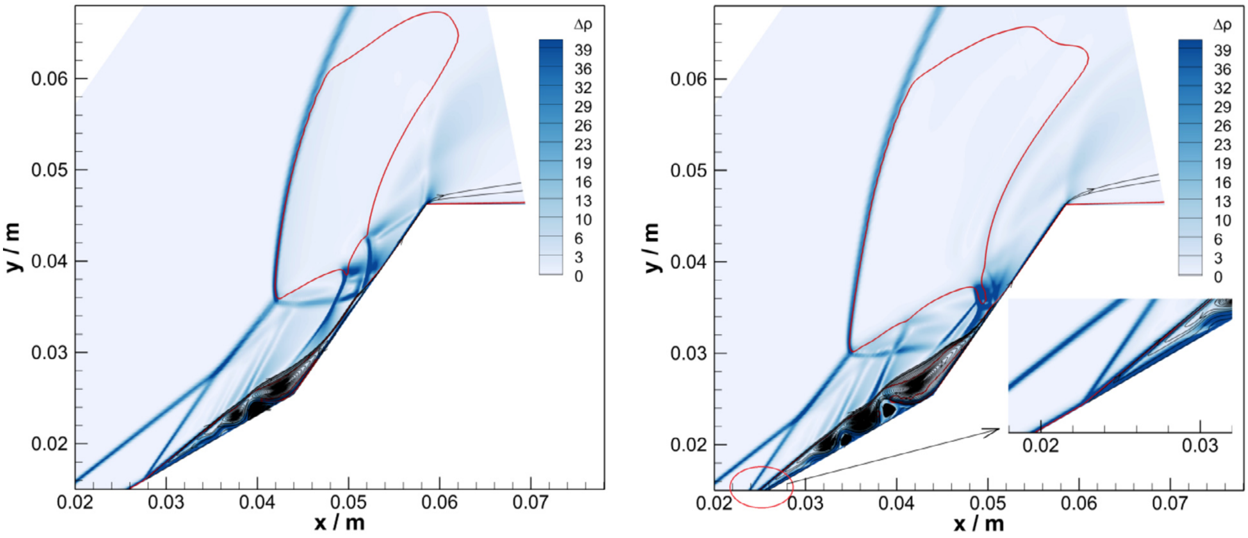

(c) CNEG

(c) TPG

Fig. 7. Density gradients of laminar flow for four models. (For interpretation of the colors in the figure(s), the reader is referred to the web version of this article.)

Thus, the shock structure in laminar flow for the TCNEG model is close to Edney type-IV interaction.

From Fig. 7(a) and Fig. 7(c), the shock structures for the TCNEG and CNEG models are similar. Yet, the reflected shock for the CNEG model is stronger than that for the TCNEG model since its reattachment shock is closer to the back wedge, meaning that the local heat flux for the CNEG model is higher near the reflected shock. The number and area of vortices for the CNEG model are smaller than the other models. From Fig. 7(b) and Fig. 7(d), the shock structures for the TNCFG and TPG models are similar. Their reattachment shocks are closer to the back wedge than other two models, and intersect with the reflected shocks. Hence, their shock interactions near the back wedge are stronger than other two models, and the shock interaction for the TPG model is the strongest since its reattachment shock is closest to the back wedge.

Fig. 8 shows the Mach number contours of laminar flow for the four gas models. For the TCNEG model, there are extensive low-velocity regions downstream of the detached shock. The slip-line above the transmitted shock intersects with the reattached shock and the reflected shock of the transmitted shock, then two deflections occur. There is an supersonic jet between the slip-line and the back wedge. Compared with the CNEG model, the slip-line for the TCNEG model is farther from the back wedge, which mean that the area of supersonic jet for it is wider. For the TNCFG and TPG models, the transmitted shock weakens into a compression wave when it intersects with the strong shock caused by the larger primary vortex at the corner of the two wedges; The deflection point of their slip-line is closer to the back wedge than other two models; Their larger primary vortexes lead to the more compression and expansion waves on the slip surface of the separation zone, so their wave systems above compression corner look more chaotic and more complex than those for the TCNEG and CNEG model.

Fig. 9 shows the static temperature contours of laminar flow for the four models. The peak values of static temperature for the TCNEG and TNCFG models are all about 6800 K, but those for the CNEG and TPG models are 5667 K and 6267 K, respectively. Downstream of the attached shock, the distributions of static temperature for the TCNEG and TNCFG models are close, and those for the CNEG and TPG models are also consistent, indicating that there is almost no chemical reaction here. The translational-rotational energy cannot be completely transferred to the vibrational-electronic state when the thermals state is in non-equilibrium. Therefore, the

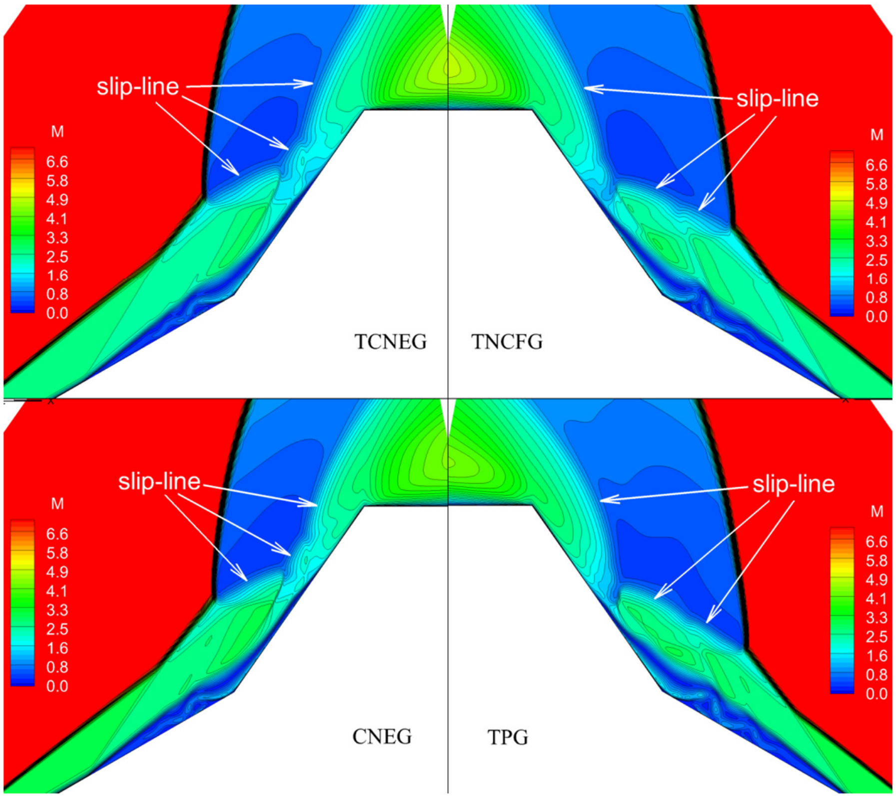

Fig. 8. Mach number contours of laminar flow for four models.

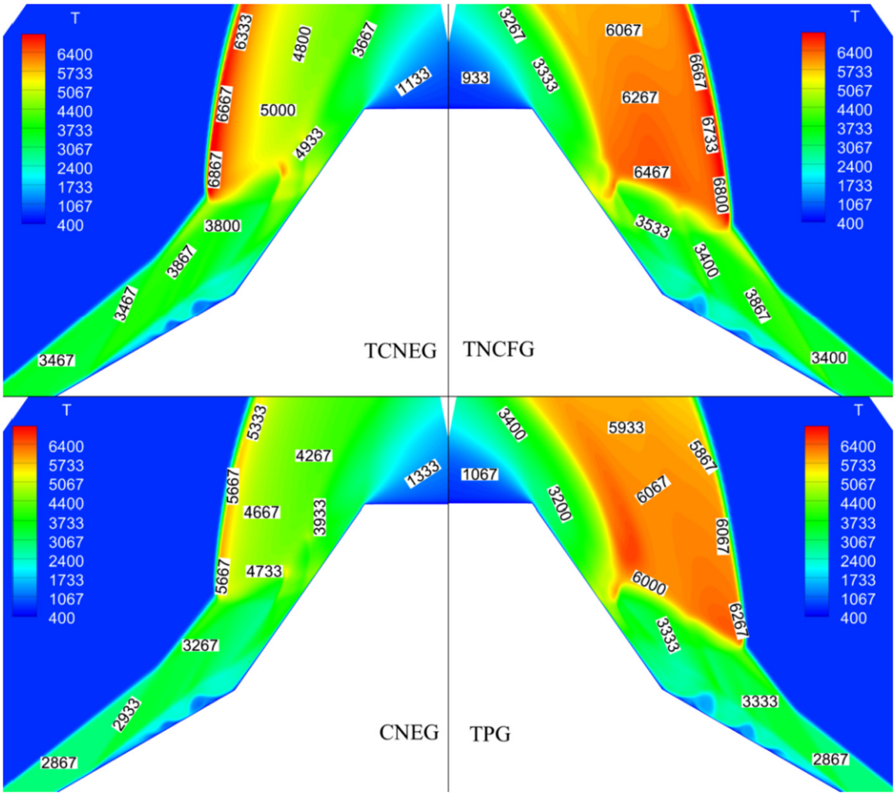

Fig. 9. Static temperature contours of laminar flow with four gas models.

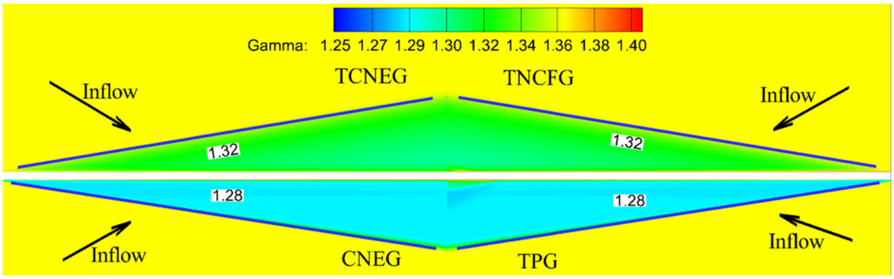

Fig. 10. Specific heat ratio downstream of attached shock (blue line) for four models.

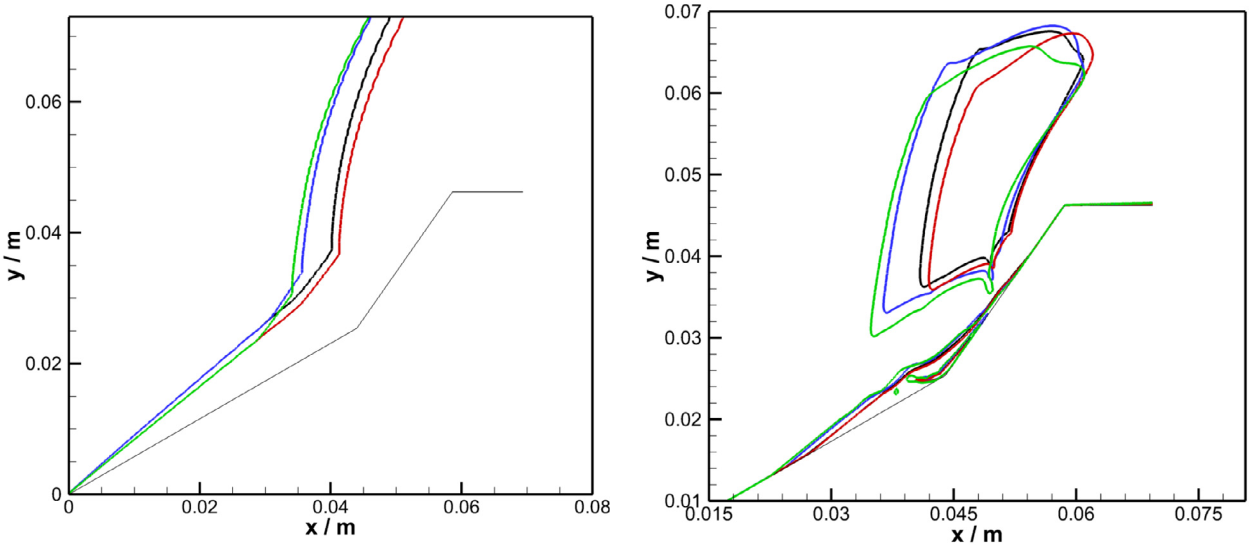

(a) Attached shock and detached shock

(b) Sonic line

Fig. 11. Comparisons of laminar flow fields for four models (TCNEG:black, TNCFG:blue, CNEG:red, TPG:green).

translational-rotational temperature (static temperature) for the TCNEG model is greater than that for the CNEG model.

Near the detached shock, the distributions of static temperature for the TCNEG and TNCFG models are almost the same, indicating that the dissociation reactions for the TCNEG model are weak here; The static temperatures for the CNEG model are lower than those for the TCNEG model, meaning that the endothermic actions of the dissociation reactions for the CNEG model are stronger. The endothermic actions of the dissociation reaction make the static temperatures for the TCNEG and CNEG models significantly lower than those for the TNCFG and TPG models in the subsonic zone downstream of the detached shock. For the TNCFG and TPG models, there is an obvious temperature boundary between the subsonic zone and the supersonic jet.

From Fig. 9, the static temperatures downstream of the attached shock for the thermal non-equilibrium gas models (TCNEG and TNCFG) are higher than the thermal equilibrium gas models (CNEG and TPG). Hence, the specific heat ratios downstream of the attached shock (blue line) for the TCNEG and TNCFG models are higher compared to the other models, which can be seen from Fig. 10.

Fig. 11 shows the comparisons of the laminar flow fields for the four models. The attached shock positions for the TCNEG and TNCFG models are closer to the upstream than the other models due to the higher specific heat ratios. Compared with the TNCFG and TPG models, the endothermic actions of the dissociation reactions make the standoff distance of the detached shock for the TCNEG and CNEG models smaller, so their subsonic region areas are also obviously smaller. The triple point and adverse pressure region are closer to the downstream, causing their separation shock to be also closer to the downstream. The standoff distance of the detached shock for the TPG model is the largest, and its subsonic region after the detached shock is the broadest and separation shock position is closest to the upstream. The detached shock for the CNEG model is closest to the downstream, and its subsonic region after the detached shock is the narrowest.

3.2. Analysis of non-equilibrium effects in laminar flow

Fig. 12 shows the vibrational-electronic temperature contours of laminar flow for the TCNEG and TNCFG models. The peak values of the vibrational-electronic temperature for the two models near the detached shock are 3733 K and 4600 K, respectively. In the subsonic region downstream of the detached shock, the peak values of the vibrational-electronic temperatures for the two models are 4133 K and 6333 K, respectively. The vibrational-electronic temperature for the TCNEG model remains unchanged at 4133 K along the flow direction, while that for the TNCFG model gradually decreases. The vibrational-electronic temperatures for the two models in supersonic jet are 4000 K and 4600 K, respectively. On the whole, downstream of the detached shock, the vibrational-electronic temperature for the TCNEG model is all less than that for the TNCFG model, meaning that the dissociation reactions consume some vibration-electronic energies here.

To better understand the energy transfer between the translational-rotational and vibrational-electronic states in the double-wedge flow, Fig. 13 shows the ratios of T_{tr} to T_{ve} in laminar flow for the TCNEG and TNCFG models. Near the attached shock and the detached shock, the ratios of T_{tr} to T_{ve} for the two models

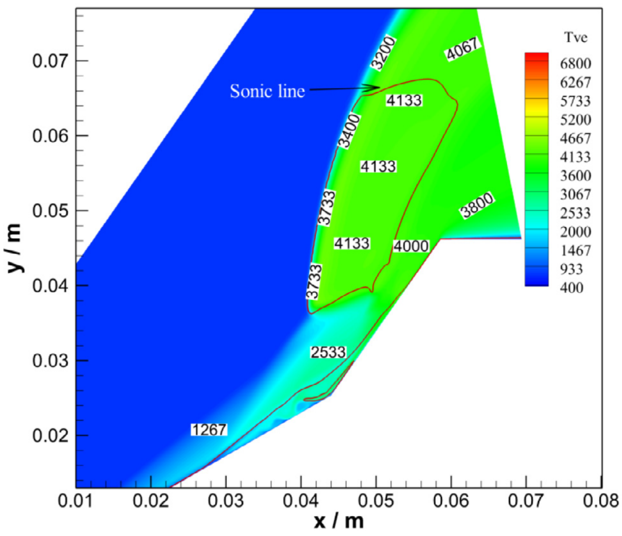

(a) TCNEG

(b) TNCFG

Fig. 12. T_{ve} contours of laminar flow for TCNEG and TNCFG models.

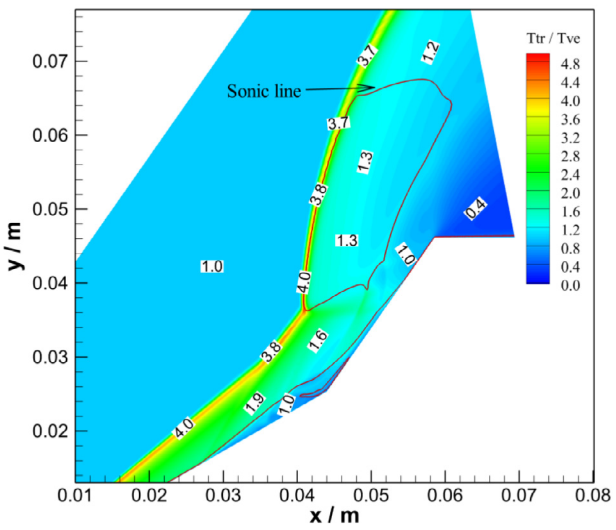

(a) TCNEG

(b) TNCFG

Fig. 13. Ratios of T_{tr} to T_{ve} in laminar flow for TCNEG and TNCFG models.

are closed to 4 and the largest, meaning that the thermal non-equilibrium effect is the strongest here. The ratios of T_{tr} to T_{ve} of the two gas models are closed to 2.0 downstream of the attached shock. Downstream of the detached shock, the ratio of T_{tr} to T_{ve} for the TCNEG model is 1.3, while that for the TNCFG model is 1, which shows the influence of the dissociation reactions on the thermal non-equilibrium effects. Compared with the downstream of the detached shock, the static temperature downstream of the attached shock is lower slowing its vibration relaxation, and the flow in that is faster causing thermal non-equilibrium effect to be stronger. Expansion waves downstream of the expansion corner lead to the static temperature decreases rapidly and the vibrational-electronic energy relaxation slow. Therefore, the vibrational-electronic temperatures are higher than translational-rotational temperatures for the two models.

Fig. 14 shows the oxygen mass fraction of laminar flow for the TCNEG and CNEG models, the lower the oxygen content, the stronger the oxygen dissociation reaction. Downstream of the sonic line near the detached shock, oxygen for the CNEG model dissociates immediately, but the oxygen dissociation reaction of the TCNEG model was relatively delayed due to the slow vibration relaxation of oxygen. In the subsonic region near the slip-line, the oxygen mass fraction for the two gas models is the lowest, which is 0.05 and 0.03, respectively. Hence, it can be inferred that the oxygen dissociation reaction is the strongest here. Compared with the TCNEG model, the domain where the oxygen amount is less for the CNEG model is more extensive, meaning that the oxygen dissociation reaction for the CNEG model is stronger than that for the TCNEG model in the low-velocity region downstream of the detached shock. The oxygen dissociation reactions of the two models are all weaker in the supersonic jet and expansion region.

Fig. 15 shows the nitrogen mass fraction of laminar flow for the TCNEG and CNEG models. In the subsonic region, the nitrogen mass fraction for the two models is the lowest, which is 0.739 and 0.754, respectively. Maximum dissociation degrees of nitrogen for the two models are 0.065 and 0.044, respectively. Obviously, the dissociation reaction of nitrogen is weaker than that of oxygen. The nitrogen dissociation reaction for the TCNEG model is stronger

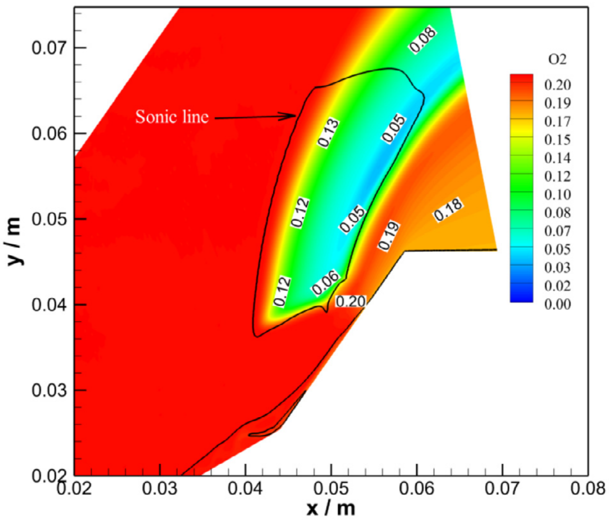

(a) TCNEG

(b) CNEG

Fig. 14. Oxygen mass fraction of laminar flow for TCNEG and CNEG models.

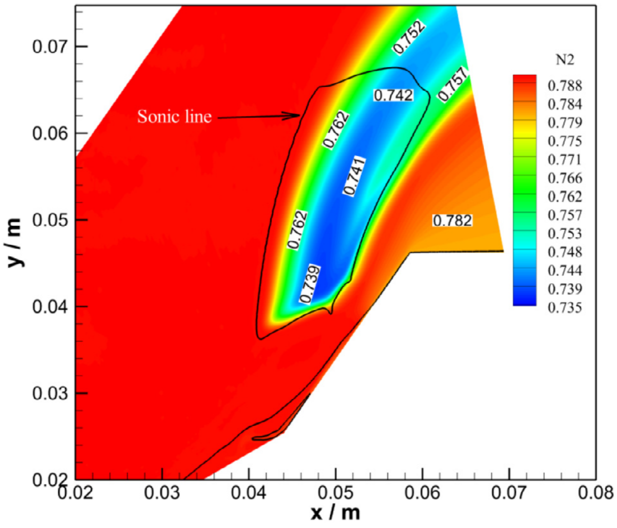

(a) TCNEG

(b) CNEG

Fig. 15. Nitrogen mass fraction of laminar flow for TCNEG and CNEG models.

than that for the CNEG model in the subsonic region downstream of the detached shock.

Through comparing the dissociation reactions for the TCNEG and CNEG models, it can be found that oxygen dissociation reaction is stronger for the CNEG model, whereas the nitrogen dissociation reaction is stronger for the TCNEG model, which is similar to the results in reference [36]. The reason for the above difference should be that the inverse reaction of each elementary reaction is considered, and the decrease of oxygen is conducive to the recombination of nitrogen.

3.3. Analysis of flow-field in turbulence flow

The Spalart-Allmaras model [25] is used to predict the double-wedge flow-fields in turbulent flow, Other calculation details are consistent with Section 3.1. In order to compare with the laminar flow, the turbulent numerical results at 170 μs are selected for analysis.

Fig. 16 shows the density gradients of turbulent flow for the four models. The shock structure for the TCNEG model is analyzed firstly. Downstream of the detached shock, the red solid line represents the sonic line. The detached shock is closer to positive shock, so the shock structure in turbulent flow is closer to Edney type-IV interaction. From Fig. 16(c), the separation shock near the compression corner for the CNEG model and the reattachment shock merge into a stronger shock, then intersects the transmitted shock; This intersection is closest to the back wedge compared to the other models, causing that its shock interaction near the back wedge is the strongest. Besides, the reflected shock for the TPG model is stronger than the TCNEG and TNCFG models, that for the TCNEG model is the weakest among the four models.

Fig. 17 shows the Mach number contours of turbulent flow for the four models. The separation zones for each model in the turbulent flow are smaller than those in the laminar flow. The separation shock intersects with the transmitted rather than the attached shock. The separation zones for the CNEG model are the smallest, only two small local separation zones occur at the corner

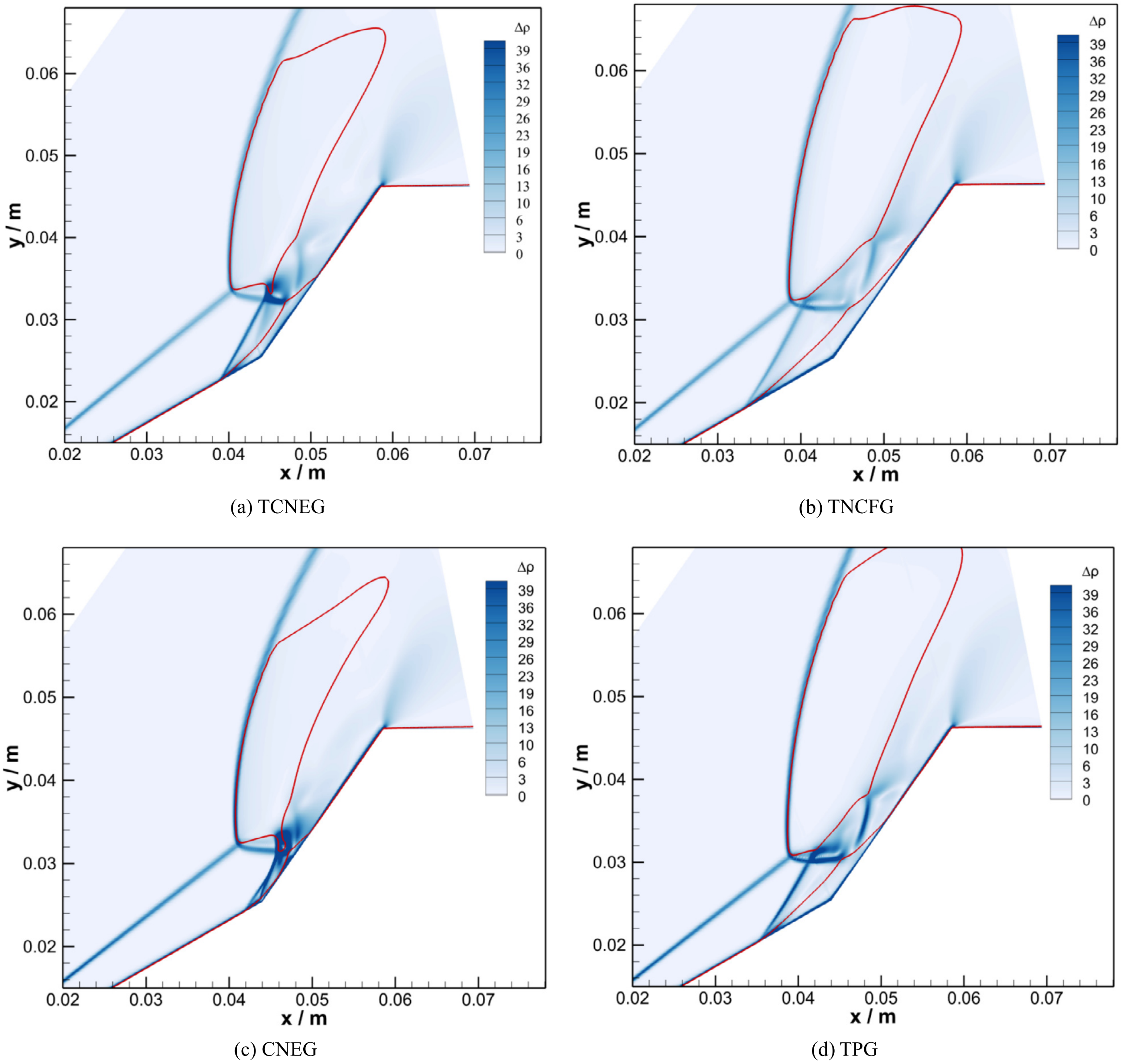

(a) TCNEG
(b) TNCFG
(c) CNEG
(d) TPG

Fig. 16. Density gradients of turbulent flow for four models.

of the two wedges and the intersection of the transmitted shock on the back wedge. The separation zone for the TNCFG model is the largest, and the intersection of the separation shock and transmitted shock is closest to the triple point. For the TCNEG and CNEG models, there is a local sonic region after the separation shock intersects with the transmission shock, followed by supersonic jet. For the TNCFG and TPG models, the flow is supersonic from the separation shock to the expansion corner.

Because the separation shock does not intersect with the attached shock (Fig. 17), it can not change the position of the triple point. The positions of the detached shock for the TNCFG and TPG models are almost the same (Fig. 18(a)). Compared to the TPG model, the static temperature for the TNCFG model with the thermal non-equilibrium effects is higher, causing that its wall shear stress is smaller. So, and its separation shock position is closer to upstream (Fig. 18(b)). Due to the stronger dissociation reactions, the position of the detached shock for the CNEG model is the closest to the downstream, the areas of the subsonic zone after its detached shock and its separation zone are minimal.

There is little difference between the temperature characteristics (including static temperature and vibrational-electronic temperature) in the turbulence and laminar flows, so those are not analyzed in detail. Fig. 19 shows the oxygen mass fraction of the turbulent flow for the TCNEG and CNEG models. In the subsonic zone near the slip-line, the oxygen mass fraction for the two gas models are the lowest, which is 0.06 and 0.04, respectively. In the supersonic jet, the lowest oxygen mass fraction for the two gas models are 0.17 and 0.13, respectively; The oxygen content for the TCNEG model gradually decreases along the flow direction, while that for the CNEG model remains unchanged. Compared with the laminar flow, the oxygen dissociation reaction in the supersonic jet for turbulence flow is stronger. Overall, the oxygen dissociation reaction for the CNEG model is also stronger than that for the TCNEG model.

Fig. 20 shows the nitrogen mass fraction of the turbulent flow for the TCNEG and CNEG models. In the subsonic zone, the nitrogen mass fractions for the two models are the lowest, which is 0.739 and 0.754, respectively. In the supersonic jet, the lowest

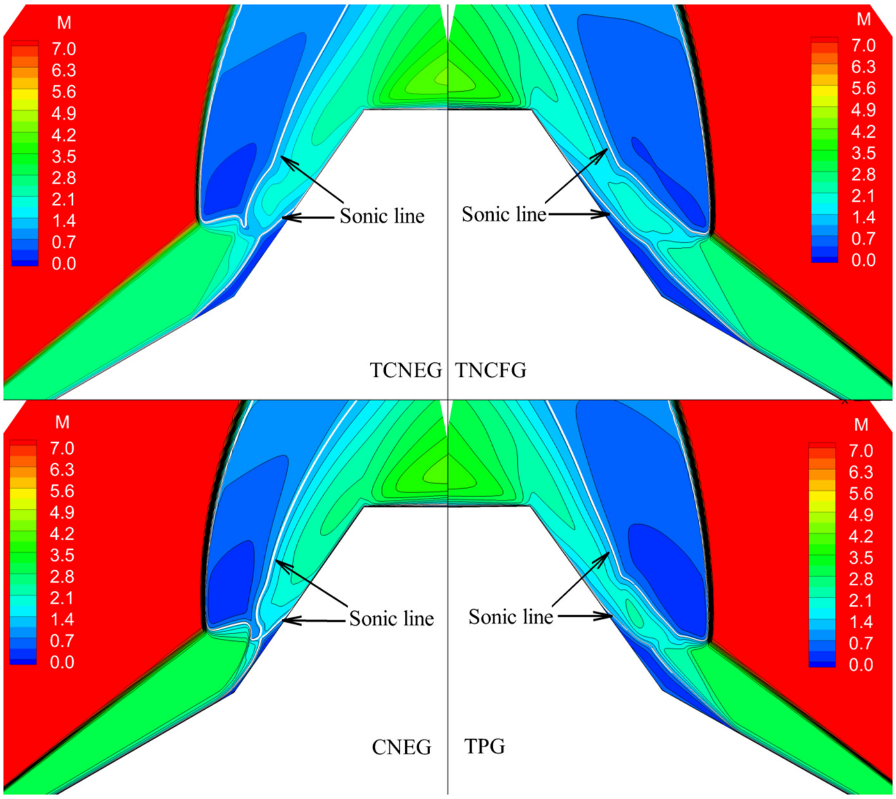

Fig. 17. Mach number contours of turbulent flow for four models.

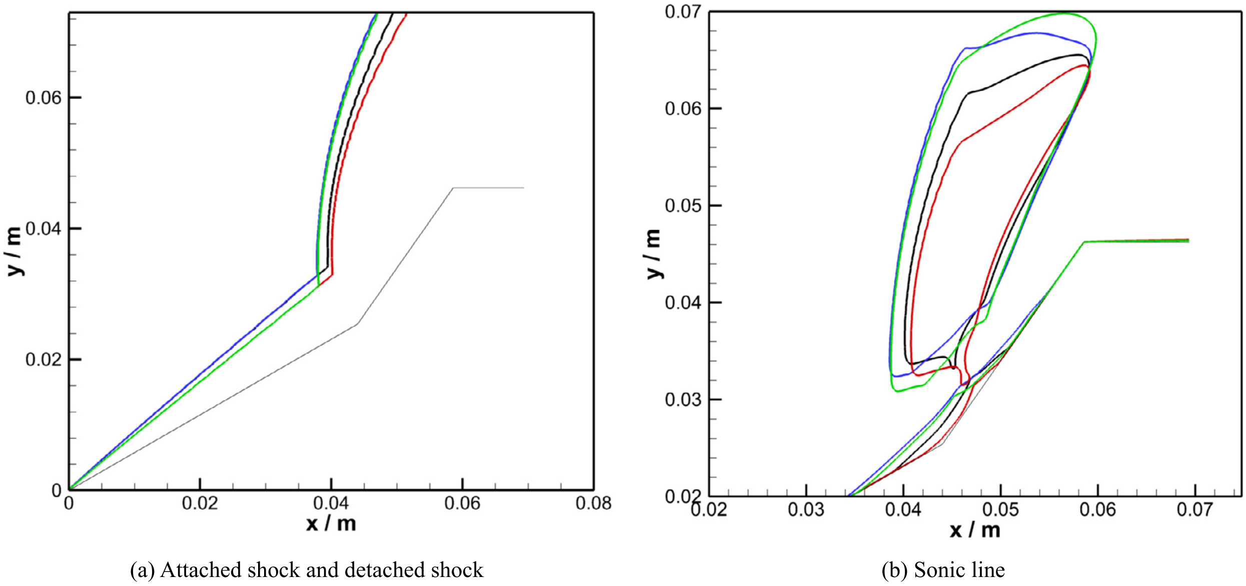

(a) Attached shock and detached shock

(b) Sonic line

Fig. 18. Comparisons of turbulence flow fields for four models (TCNEG:black, TNCFG:blue, CNEG:red, TPG:green).

oxygen mass fraction for the two gas models are 0.780 and 0.774, respectively. Compared with the laminar flow, the nitrogen dissociation reaction in the subsonic region for turbulence flow is also weaker, but that in the supersonic jet for turbulence flow is also stronger.

To better explain the difference of dissociation reactions between laminar and turbulence flows, Fig. 21 shows the shock positions of the laminar (blue) and turbulent (red) flows for the TCNEG model and Fig. 22 shows x direction velocity for the TCNEG model on the section of y = 0.0463 m. The separation shock interacts with the detached shock in the laminar flow but with the transmitted shock in the turbulent flow. So, the triple point of the turbulence flow is closer to upstream than the laminar flow (Fig. 21), meaning that its detached shock intensity in front of the back wedge is weaker. Hence, x direction velocity after the detached shock of the turbulence flow is higher than the laminar flow (Fig. 22). It can be deduced that the faster flows in the subsonic region for the turbulence flow should be the reason why the oxygen and nitrogen dissociation reactions of it weaker than the laminar flow.

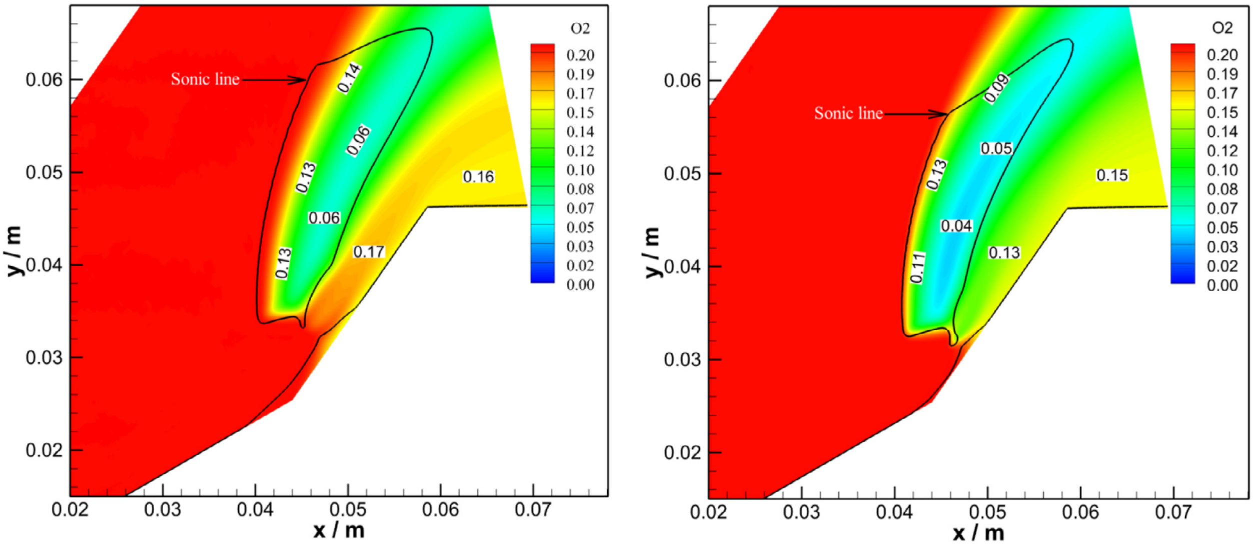

(a) TCNEG (b) CNEG

Fig. 19. Oxygen mass fraction of turbulent flow for TCNEG and CNEG models.

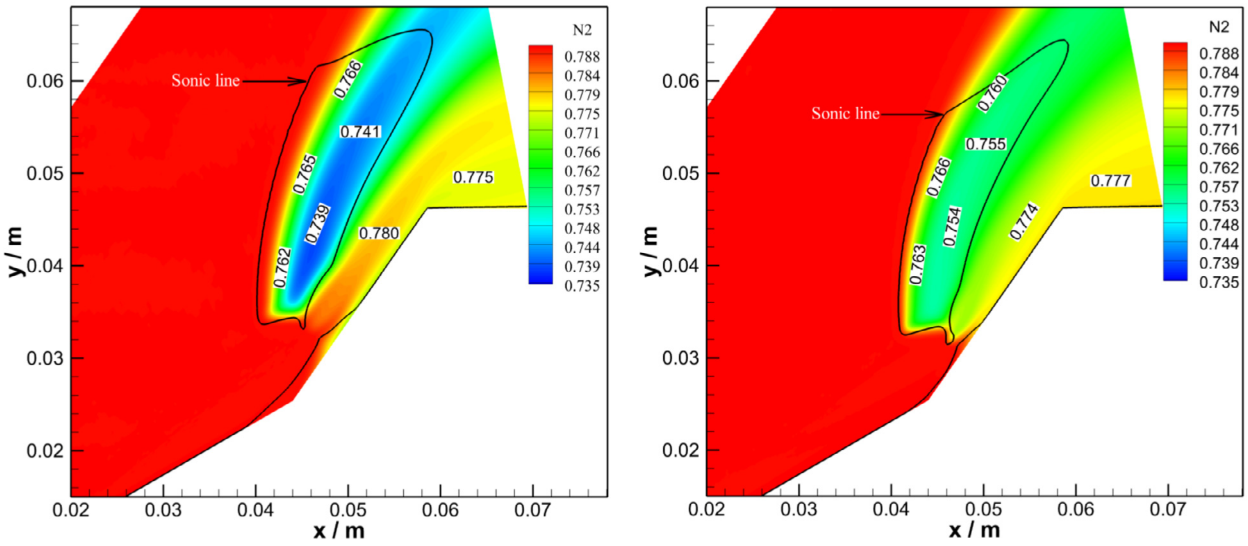

(a) TCNEG (b) CNEG

Fig. 20. Nitrogen mass fraction of turbulent flow for TCNEG and CNEG models.

3.4. Analysis of wall parameters

To better understand the differences between the four gas models, the wall parameters including static pressure and heat flux are used for the quantitative analysis. Fig. 23 shows the wall parameters of double-wedge in the laminar flow. The separation zones for the TPG, CNEG, TNCFG, and TCNEG models start at $x = 0.0225$ m, 0.0266 m, 0.245 m, and 0.273 m, respectively. There are different size vortices in the separation zone, which causes the distributions of the heat flux and static pressure at the wall oscillate irregularly at x = 0.03 - 0.05 m. The peak values of heat flux for the TPG and TNCFG models are 16.2 MW/m^2 and 15 MW/m^2, respectively, which are higher than the experimental values [17], but their positions are closer to the upstream than the experimental result [17]. The peak values of heat flux for the CNEG and TCNEG models are 11 MW/m^2 and 9.4 MW/m^2, which are closed to the experimental values. Importantly, the values and positions of the heat flux peak are consistent with the experiment [17]. Since the reflected shock on the back wedge for the CNEG model is stronger and its thermal state is in equilibrium, the peak value of its heat flux is higher than that for the TCNEG model. Due to the endothermic effect of dissociation reactions, the peak values of heat flux for the CNEG and TCNEG models are about 26.7% - 41.3% lower than those for the TPG and TNCFG models, the peak values of static pressure for the CNEG and TCNEG models are about 11.1% - 23.1% lower than those for the TPG and TNCFG models. Since the shock interaction near the back wedge for the TPG model is the strongest (Fig. 16), the peak value of its heat flux is the highest. The peak values of heat flux for the four models might depend on the intensity of the reflected shock on the back wedge and its nearby shock interaction, and the details can be seen in the analysis of Fig. 3.

Fig. 24 shows the wall parameters of double-wedge in the turbulence flow. The separation zones for the TPG, CNEG, TNCFG, and TCNEG models start at $x = 0.353$ m, 0.418 m, 0.332 m, and 0.388 m, respectively. The starting position of the separation zone for the TNCFG model is the most upstream, which can also be seen

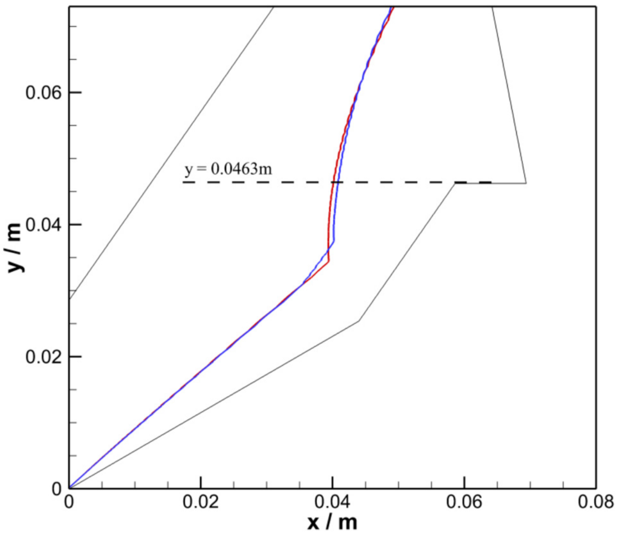

Fig. 21. Shock positions of laminar (blue) and turbulent (red) for TCNEG model.

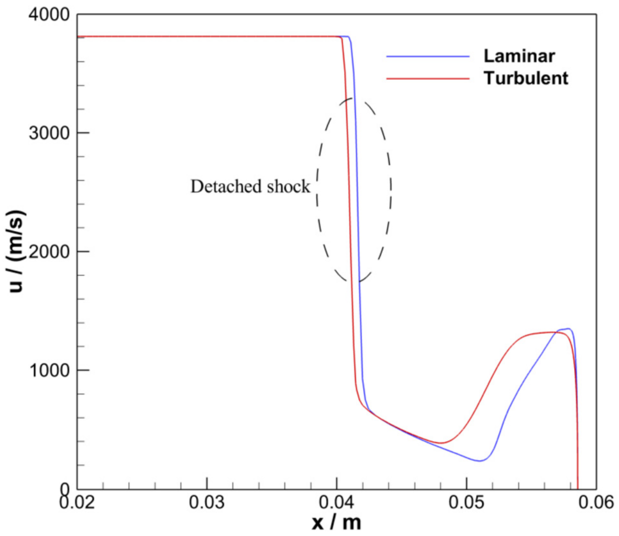

Fig. 22. x direction velocity for TCNEG model on section of y = 0.0463 m.

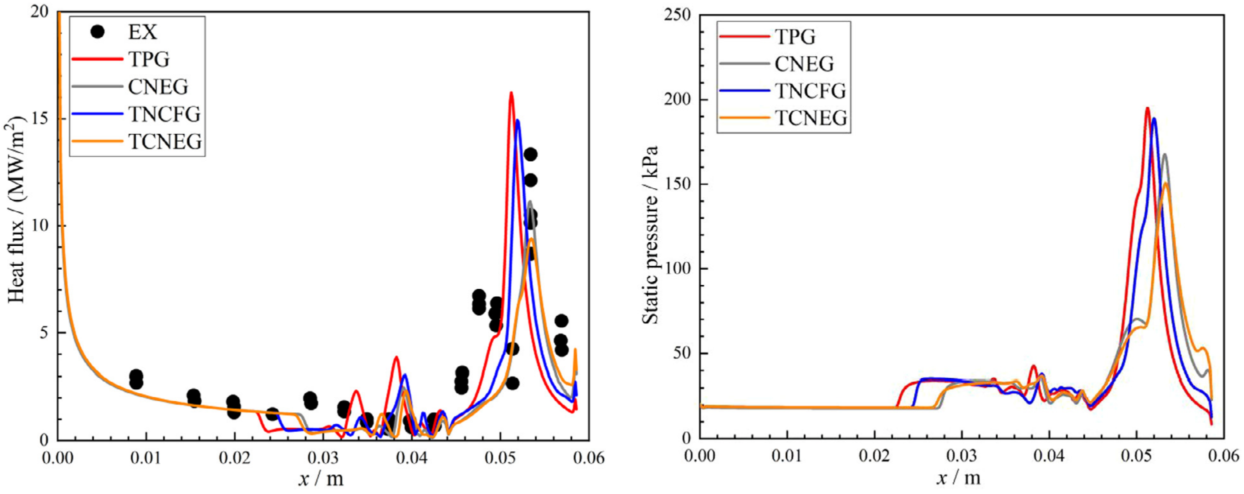

(a) Heat flux

(b) Static pressure

Fig. 23. Wall parameters of double-wedge in laminar flow.

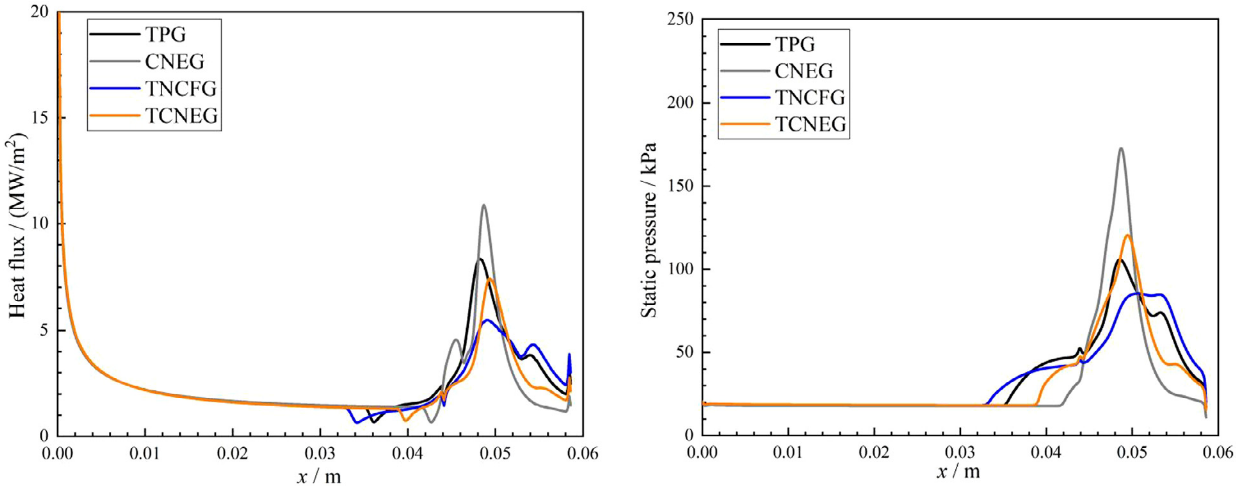

(a) Heat flux

(b) Static pressure

Fig. 24. Wall parameters of double-wedge in turbulence flow.

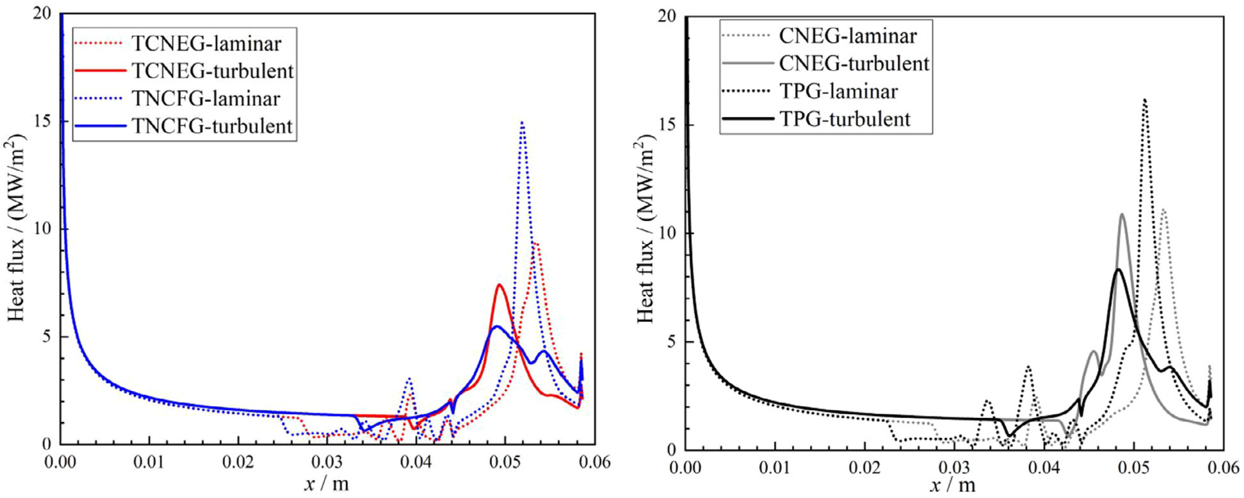

(a) TCNEG and TNCEG (b) CNEG and TPG

Fig. 25. Wall heat flux distribution of laminar and turbulent flow for four models.

in Fig. 18. Since the shock interaction near the back wedge for the CNEG model is the strongest (Fig. 16), the peak values of the heat flux and static pressure for it are the highest. The peak positions of heat flux and static pressure for the TPG model are closest to upstream. Compared with the TPG model, the peak value of the heat flux for the TCNEG model is lower due to its weaker reflected shock on the back wedge. Unlike other models, the static pressure of the TNCFG model changes little downstream of the peak position due to its weaker reflected shock on the back wedge, and a static pressure peak platform is formed at $x = 0.050$ - 0.053 m.

Fig. 25 shows the wall heat flux distributions of the laminar and turbulent flows for the four models. Because the turbulence viscosity can not be fully developed near the wall of the double wedge with the small size and cold wall, the heat fluxes upstream of the separation zone in the turbulent flow are slightly higher than those in the laminar flow, which is for all models. The peak values of heat flux in the laminar flow are higher than those in the turbulent flow due to its stronger reflected shocks on the back wedge. The separation shocks in the turbulent flow can not change the position of the triple point and its separation zones are smaller, so the peak positions of heat flux in it are closer to upstream than those in the laminar flow.

4. Conclusions

In this study, the unsteady simulations of double-wedge flows at a total enthalpy of 8 MJ/kg are finished by using the TCNEG, TNCFG, CNEG, and TPG models. To obtain the influences of high temperature non-equilibrium effects on shock wave interaction and shock wave/boundary layer interaction in the hypervelocity laminar and turbulent flows, the flow-fields and wall parameters for the different models are compared. The main conclusions are given as follows:

(1) Although the TCNEG models over-predict the length of the separation zone, the peak value of the heat flux for it at 170 μs is about 21.89%∼52.76% higher than the reference studies. Overall, the shock structures and the peak heat flux for TCNEG model at 170 μs are agreed better with the experiment results.

(2) For laminar flow, the separation shock position for the CNEG model is the most downstream, which is close to that for the TCNEG model. The oxygen dissociation reaction for the CNEG model is stronger than that for the TCNEG model in the subsonic region downstream of the detached shock.

(3) For turbulent flow, the separation shock position for the CNEG model is quite different from that for the TCNEG model. Compared with the laminar flow, the dissociation reactions downstream of the detached shock for turbulence flow are weaker, but that in the supersonic jet for turbulence flow are stronger.

(4) The different size vortices in the separation zone for the laminar flow cause that the distributions of the wall parameters oscillate irregularly at $x = 0.030$ - 0.050 m. Since the reflected shock on the back wedge for the CNEG model is stronger and its thermal state is in equilibrium, the peak value of its heat flux is higher than that for the TCNEG model.

(5) The peak values of the heat flux for the TPG model is the highest in the laminar flow, but that for the CNEG model is the highest in the turbulent flow. The intensity of the reflected shocks on the back wedge and its nearby shock interaction largely determine the peak values of the heat flux for the four models.

(6) The heat fluxes upstream of the separation zone in the turbulent flow are slightly higher than those in the laminar flow, which is for the four models. The peak values of the heat flux in the laminar flow are higher than those in the turbulent flow due to its stronger reflected shocks on the back wedge.

Declaration of competing interest

The authors declare that they have no known competing financial interests or personal relationships that could have appeared to influence the work reported in this paper.

Acknowledgement

The authors express sincere gratitude to the projects funded by the Postgraduate Research & Practice Innovation Program of Jiangsu Province (NO. KYCX21_0338), and China Postdoctoral Science Foundation (NO. BX20200070), and Opening Foundation of National State Key Laboratory of High Temperature Gas Dynamics (NO. 2021KF07).

References

[1] W. Huang, H. Wu, Y.G. Yang, et al., Recent advances in the shock wave/boundary layer interaction and its control in internal and external flows, Acta Astronaut. 174 (2020) 103–122.

[2] D. Knighta, O. Chazotb, J. Austin, et al., Assessment of predictive capabilities for aerodynamic heating in hypersonic flow, Prog. Aerosp. Sci. 90 (2017) 39–53.

[3] J.A. Hao, C.Y. Wen, Hypersonic flow over spherically blunted double cones, J. Fluid Mech. 896 (2020) A26.

[4] W. Yao, H. Liu, L.J. Xue, et al., Performance analysis of a strut-aided hypersonic scramjet by full-scale IDDES modeling, Aerosp. Sci. Technol. 117 (2021) 106941.

[5] W.Z. Xie, Y. Jin, Y. Ge, et al., Feasibility of employing the restarting process to evaluate the self-starting ability for hypersonic inlets, Aerosp. Sci. Technol. 107 (2020) 106347.

[6] R. Saravanan, S.L.N. Desikan, K.J. Francise, et al., Experimental investigation of start/unstart process during hypersonic intake at Mach 6 and its control, Aerosp. Sci. Technol. 113 (2021) 106688.

[7] J.T. Chang, N. Li, K.J. Xu, et al., Recent research progress on unstart mechanism, detection and control of hypersonic inlet, Prog. Aerosp. Sci. 89 (2017) 1–22.

[8] J.B. Liu, X.Q. Fan, Y. Tao, et al., Experimental and numerical study on the local unstart mechanism of hypersonic inlet, Acta Astronaut. 160 (2019) 216–221.

[9] R. Saravanan, S.L.N. Desikan, K.J. Francise, et al., Experimental investigation of start/unstart process during hypersonic intake at Mach 6 and its control, Aerosp. Sci. Technol. 113 (2021) 106688.

[10] V.R.P. Sethuraman, T.H. Kim, H.D. Kim, Effects of back pressure perturbation on shock train oscillations in a rectangular duct, Acta Astronaut. 179 (2021) 525–535.

[11] X.L. Jiao, J.T. Chang, Z.Q. Wang, et al., Hysteresis phenomenon of hypersonic inlet at high Mach number, Acta Astronaut. 128 (2016) 657–668.

[12] W.Z. Xie, Y. Jin, Y. Ge, et al., Feasibility of employing the restarting process to evaluate the self-starting ability for hypersonic inlets, Aerosp. Sci. Technol. 107 (2020) 106347.

[13] C.L. Dai, B. Sun, C.S. Zhou, et al., Numerical investigation of real-gas effect of inward-turning inlet at Mach 12, Aerosp. Sci. Technol. 115 (2021) 106786.

[14] K. Zhu, L.X. Jiang, W.D. Liu, et al., Wall temperature effects on shock wave/turbulent boundary layer interaction via direct numerical simulation, Acta Astronaut. 178 (2021) 499–510.

[15] K. Zhu, W.D. Liu, M.B. Sun, Impacts of periodic disturbances on shock wave/turbulent boundary layer interaction, Acta Astronaut. 182 (2021) 230–239.

[16] A. Erb, S. Hosder, Analysis of turbulence model uncertainty for shock-wave/boundary-layer interaction simulations, J. Spacecr. Rockets 57 (2020) 1265–1283.

[17] A. Swantek, The role of aerothermochemistry in double cone and double wedge flows, Ph.D thesis, University of Illinois at Urbana-Champaign, Illinois, UK, 2012.

[18] J.A. Hao, C.Y. Wen, J.Y. Wang, Numerical investigation of hypervelocity shock-wave/boundary-layer interactions over a double-wedge configuration, Int. J. Heat Mass Transf. 138 (2019) 277–292.

[19] D. Vatansevera, B. Celik, Unsteady shock interaction mechanisms of high enthalpy reacting flows over double wedges at Mach 7, Phys. Fluids 33 (2021) 056110.

[20] O. Tumuklu, D.A. Levin, Modal analysis with proper orthogonal decomposition of hypersonic separated flows over a double wedge, Phys. Rev. Fluids 4 (2019) 033403.

[21] C. Park, Assessment of two-temperature kinetic model for ionizing air, J. Thermophys. Heat Transf. 3 (3) (1989) 233–244.

[22] C. Park, Review of chemical-kinetic problems of future NASA missions, I: Earth entries, J. Thermophys. Heat Transf. 7 (3) (1993) 385–398.

[23] C. Park, Problems of rate chemistry in the flight regimes of aeroassisted orbital transfer vehicles, Prog. Astronaut. Aeronaut. 96 (1985) 511–537.

[24] B.J. McBride, M.J. Zehe, S. Gordon, NASA Glenn coefficients for calculating thermal properties of individual species, Technical Report No. NASA/TP-2002-211556.

[25] S. Catris, B. Aupoix, Density corrections for turbulence models, Aerosp. Sci. Technol. 4 (1) (2000) 1–11.

[26] W.O. Landsberg, V. Wheatley, M.K. Smart, et al., Performance of high Mach number scramjets - tunnel vs flight, Acta Astronaut. 146 (2018) 103–110.

[27] D. Curran, V. Wheatley, M.K. Smart, Investigation of combustion mode control in a Mach 8 shape-transitioning scramjet, AIAA J. 57 (2019) 2978–2988.

[28] W.O. Landsberg, V. Wheatley, M.K. Smart, et al., Enhanced supersonic combustion targeting combustor length reduction in a Mach 12 scramjet, AIAA J. 56 (2018) 3803–3807.

[29] Y.P. Qin, P.Q. Liu, Q.L. Qu, et al., Numerical study of aerodynamic forces and flow physics of a delta wing in dynamic ground effect, Aerosp. Sci. Technol. 51 (2016) 203–221.

[30] Y.P. Qin, P.Q. Liu, Q.L. Qu, et al., Wing/canard interference of a close-coupled canard configuration in static ground effect, Aerosp. Sci. Technol. 69 (2017) 60–75.

[31] P.N. Gupta, J.M. Yos, R.A. Thompson, et al., a review of reaction rates and thermal and transport properties for an 11-species air model for chemical and thermal nonequilibrium calculations to 30000K, Technical Report No. NASA/TP-1990-1323.

[32] C.R. Wilke, A viscosity equation for gas mixtures, J. Chem. Phys. 18 (4) (1950) 517–519.

[33] P. Batten, N. Clarke, C. Lambert, et al., On the choice of wavespeeds for the HLLC Riemann solver, SIAM J. Sci. Comput. 18 (1997) 1553–1570.

[34] A. Harten, High resolution schemes for hyperbolic conservation laws, J. Comput. Phys. 49 (1983) 357–393.

[35] J.R. Komives, I. Nompehv, G.V. Candler, Numerical investigation of unsteady heat transfer on a double wedge geometry in hypervelocity flows, in: 44th AIAA Fluid Dynamics Conference, AIAA Aviation, 16–20 June, Atlanta, GA, 2014.

[36] H. Jiang, J. Liu, S. Luo, et al., Thermochemical non-equilibrium effects on hypersonic shock wave/turbulent boundary-layer interaction, Acta Astronaut. (2022) 1–14.